GEOPHYSICS, VOL. 70, NO. 1 (JANUARY-FEBRUARY 2005); P. S30–S37, 6 FIGS.
10.1190/1.1852787

Multicomponent prestack depth migration using the elastic screen method

Xiao-Bi Xie[1] and Ru-Shan Wu[1]

ABSTRACT

A 3D multicomponent prestack depth-migration method is presented. An elastic-screen propagator based on one-way wave propagation with a wide-angle correction is used to extrapolate both source and receiver wavefields. The elastic-screen propagator neglects backscattered waves but can handle forward multiple-scattering effects, such as focusing/defocusing, diffraction, interference, and conversions between P- and S-waves. Vector-imaging conditions are used to generate a P-P image and a P-S converted-wave image. The application of the multicomponent elastic propagator and vector-imaging condition preserves more information carried by the elastic waves. It also solves the polarization problem of converted-wave imaging. Partial images from different sources with correct polarizations can be stacked to generate a final image. Numerical examples using 2D synthetic data sets are presented to show the feasibility of this method.

INTRODUCTION

Recent developments in multicomponent seismic acquisition, such as ocean-bottom cable technology, significantly increase the information in the data. From multicomponent seismic data, both P-P and P-S sections can be obtained. Because these waves carry different information about target regions, they may provide estimates of petrophysical parameters that cannot be obtained with P-wave data alone. However, more sophisticated imaging/inversion techniques are required in order to extract the new information.

Several types of methods have been proposed for elastic-wave migration. Chang and McMechan (1987, 1994) conducted 2D and 3D elastic reverse-time migrations using a full-wave finite-difference method. Kirchhoff elastic-wave migration was implemented by Kuo and Dai (1984) and by Dai and Kuo (1986). Hokstad (2000) recently proposed a multicomponent Kirchhoff-migration method and imaging conditions for multicomponent data. Zhe and Greenhalgh (1997) used potentials instead of displacements to propagate P- and S-waves. Some authors (e.g., Jin et al., 1998b; Sun and McMechan, 2001; Hou and Marfurt, 2002) treated P- and S-waves as scalar waves with different velocities and used a scalar-wave propagator for the migration. For existing elastic-wave-migration approaches, the reverse-time propagator based on the full-wave finite-difference method is accurate. However, the method is usually very time consuming, especially in 3D. The ray-based Kirchhoff method is efficient and can carry polarization information of multicomponent waves but has difficulty dealing with many wave-related phenomena. The potential approach by Zhe and Greenhalgh (1997) is very attractive. It uses a scalar potential to propagate elastic waves, then retrieves vector waves from the potentials. However, in 3D, the S-wave potential itself is a 3D vector field, which reduces the advantage of this approach. Using a scalar-wave propagator to simulate elastic-wave propagation, although straightforward, loses polarization information carried in the multicomponent wavefield unless otherwise specially treated (Hou and Marfurt, 2002).

The phase-screen method, or split-step Fourier method (Stoffa et al., 1990), is based on the one-way wave equation. It can properly handle wave motion–related phenomena. Although the original phase-screen method cannot handle large scattering angles under large velocity perturbations, several modifications have been developed to improve its accuracy for wide angles and large velocity contrasts (e.g., Ristow and Ruhl, 1994; Jin et al., 1998a; Xie and Wu, 1998; Huang et al., 1999; Huang and Fehler, 2000; Xie et al., 2000; Biondi, 2002). By processing the wavefield in both space and wavenumber domains, the screen method is also highly efficient. It provides a fast, high-quality propagator that has been successfully used for scalar-wave migration.

The scalar-wave-screen propagator has been extended for elastic modeling of the propagation of multicomponent waves. To generalize the scalar-wave-screen propagator to the multicomponent elastic case, Fisk and McCartor (1991) derived the coupling term between P- and S-waves. Wu (1994, 1996)

Manuscript received by the Editor December 26, 2001; revised manuscript received July 6, 2004; published online January 14, 2005.
[1]University of California, Institute of Geophysics and Planetary Physics, Santa Cruz, California 95064. E-mail: xie@es.ucsc.edu; wrs@es.ucsc.edu.

derived these couplings based on the elastic scattering theory. Wild and Hudson (1998) reached a similar result using a geometric approach. Xie and Wu (1996, 2001) gave equations for modeling forward propagation and reflection of multicomponent elastic waves. Similar to a scalar-screen propagator, the elastic-screen propagator neglects reverberations between screens but can handle forward multiple-scattering effects, e.g., focusing/defocusing, diffraction, interference, and conversions between different wave types. As in the scalar-wave case, the original elastic-screen method is derived from a small-angle approximation. Xie and Wu (1999) introduced a wide-angle correction for the elastic-screen method. Their result improved the accuracy of the elastic-screen method for wide scattering angles and large velocity contrasts. Wu and Xie (1994) tested the elastic-screen method as a back propagator for multicomponent elastic migration.

Based on the successful application of scalar-wave-screen migration and development of the elastic-wave-screen propagator in seismic wave modeling, we developed a multicomponent migration method based on the elastic-screen propagator. The elastic-screen propagator retains the advantages of the original scalar-screen method and provides an efficient approach for multicomponent migration. In this paper, we first present the formulation of the elastic-screen propagator for wavefield extrapolation. Wide-angle corrections for handling wide scattering angles under large velocity contrasts are introduced. Then, vector-image conditions for multicomponent P-P and P-S wave imaging are proposed. To show the feasibility of the new migration method, several 2D synthetic data sets are generated using a full-wave finite-difference method, and multicomponent migrations are conducted using these synthetic data sets.

SCREEN PROPAGATOR FOR MULTICOMPONENT ELASTIC WAVES

Xie and Wu (2001) gave derivations of the complex-screen method for elastic-wave forward propagation and reflection. Several versions of the propagators were given, based on different approximations. To give equations for multicomponent elastic migration, we will follow the derivation in Xie and Wu (2001). Only the relevant formulation is given here, without detailed derivations. To formulate the problem in a 3D heterogeneous structure, the model is divided into a sequence of horizontally layered heterogeneous thin slabs. The geometry of the model is shown in Figure 1. For simplicity, only one thin slab is marked in the figure. For analyzing wave propagation based on the one-way wave equation, the vertical direction is chosen as the main propagation direction. We use $\mathbf{x} = \mathbf{x}_T + z\hat{\mathbf{e}}_z$ as a position vector, where $\mathbf{x}_T = x\hat{\mathbf{e}}_x + y\hat{\mathbf{e}}_y$ is a position vector in the horizontal plane, subscript T denotes the horizontal or "transverse" direction perpendicular to the main propagation direction, and z is the vertical coordinate with positive direction downward. Consider forward-propagated P- and S-waves entering the slab from the horizontal plane at z_0. After the incident waves pass through the thin slab between z_0 and z_1, and interacts with the heterogeneities within it, there will be both incident waves and different types of forward-scattered waves at the exit plane at z_1 (see Figure 1). In the frequency domain, the wavefield at z_1 can be expressed as a superposition of plane P- and S-waves

$$\mathbf{u}(\mathbf{x}_T, z_1) = \frac{1}{4\pi^2}\int d\mathbf{K}_T[\mathbf{u}^P(\mathbf{K}_T, z_1)+\mathbf{u}^S(\mathbf{K}_T, z_1)]e^{i\mathbf{K}_T\cdot\mathbf{x}_T}, \tag{1}$$

where $\mathbf{u}$ is the displacement field, superscripts P and S denote P- and S-waves, and $\mathbf{K}_T$ is the horizontal wavenumber of plane waves. For simplicity, the apparent frequency dependency has been omitted from equation 1 and following equations. If the slab is thin enough, the local Born approximation can be applied. By further invoking the small-angle approximation, the heterogeneous slab can be approximated by a homogeneous slab with background elastic parameters (P- and S-wave speeds, densities, etc.), plus a 2D heterogeneous "screen" in the horizontal direction. The screen concentrates all perturbations of elastic parameters into a sheet, i.e., 2D heterogeneities without vertical structure. The interaction between the incoming wave and a heterogeneous slab can be replaced with two separated steps: the propagation in a homogeneous slab and the interaction with a 2D heterogeneous screen. Later, as we will demonstrate, such a treatment provides an efficient way to propagate elastic waves in heterogeneous models. Based on the above treatment, plane **P**- and **S**-waves $\mathbf{u}^P(\mathbf{K}_T, z_1)$ and $\mathbf{u}^S(\mathbf{K}_T, z_1)$ at the exit plane at z_1 can be expressed as (see Xie and Wu, 2001)

$$\mathbf{u}^P(\mathbf{K}_T, z_1) = e^{i\gamma_\alpha \Delta z}\big[\mathbf{u}_0^P(\mathbf{K}_T, z_0) + \mathbf{U}^{PP}(\mathbf{K}_T, z_0) + \mathbf{U}^{SP}(\mathbf{K}_T, z_0)\big], \tag{2}$$

$$\mathbf{u}^S(\mathbf{K}_T, z_1) = e^{i\gamma_\beta \Delta z}\big[\mathbf{u}_0^S(\mathbf{K}_T, z_0) + \mathbf{U}^{SS}(\mathbf{K}_T, z_0) + \mathbf{U}^{PS}(\mathbf{K}_T, z_0)\big], \tag{3}$$

where $\Delta z = z_1 - z_0$ is the thickness of the slab, $\gamma_\alpha = (k_\alpha^2 - K_T^2)^{1/2}$ and $\gamma_\beta = (k_\beta^2 - K_T^2)^{1/2}$ are vertical wavenumbers for P- and S-waves in the background media, $k_\alpha = \omega/\alpha_0$ and $k_\beta = \omega/\beta_0$ are P- and S-wavenumbers in the background medium, and α_0 and β_0 are background P- and S-wave velocities,

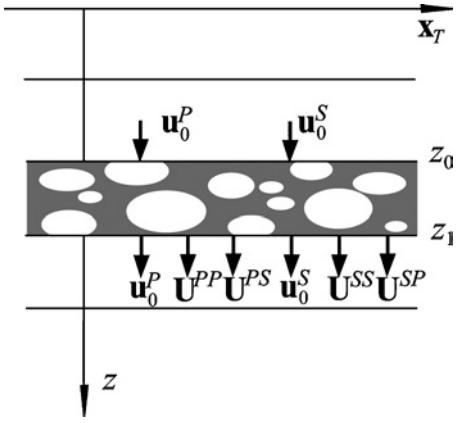

Figure 1. A sketch showing incident P- and S-waves and various types of scattered waves after they interact with a horizontal, inhomogeneous thin slab. At the entrance plane at z_0, there are incident P-wave $\mathbf{u}_0^P$ and incident S-wave $\mathbf{u}_0^S$. At the exit plane at z_1, after interacting with the inhomogeneous slab, there are incident waves and scattered waves. $\mathbf{U}^{PP}$ and $\mathbf{U}^{PS}$ are scattered P- and S-waves generated by the incident P-wave, and $\mathbf{U}^{SP}$ and $\mathbf{U}^{SS}$ are scattered P- and S-waves generated by the incident S-wave.

respectively. In the above equations, $\mathbf{u}_0$ is the incident wavefield at the entrance plane at $z = z_0$. Their superscripts P and S denote P- and S-waves. $\mathbf{U}$ denotes scattered waves. These scattered fields are generated by the interaction between incident waves and heterogeneities in the slab. $\mathbf{U}^{PP}$ and $\mathbf{U}^{PS}$ are scattered P- and S-waves generated by the incident P-wave, and $\mathbf{U}^{SP}$ and $\mathbf{U}^{SS}$ are scattered P- and S-waves generated by the incident S-wave. Phase-shift factors $\exp(i\gamma_\alpha \Delta z)$ and $\exp(i\gamma_\beta \Delta z)$ propagate wavefields through the homogeneous background. Equations 2 and 3 indicate that, at the exit plane, the new P-wave is composed of an incident P-wave and scattered P-waves from incident P- and S-waves, and the new S-wave is composed of an incident S-wave and scattered S-waves from incident P- and S-waves. The process is sketched in Figure 1. For an isotropic medium, the scattered fields in equations 2 and 3 can be expressed as (Xie and Wu, 2001)

$$\mathbf{U}^{PP}(\mathbf{K}_T, z_0) = -ik_\alpha \Delta z \hat{k}_\alpha \eta^{PP} \iint d\mathbf{x'}_T e^{-i\mathbf{K}_T \cdot \mathbf{x'}_T} \times u_0^P(\mathbf{x'}_T, z_0) \frac{\delta\alpha(\mathbf{x'}_T)}{\alpha_0}, \tag{4}$$

$$\mathbf{U}^{PS}(\mathbf{K}_T, z_0) = -ik_\beta \Delta z \eta^{PS} \hat{k}_\beta \times \left\{ \hat{k}_\beta \times \iint d\mathbf{x'}_T \times e^{-i\mathbf{K}_T \cdot \mathbf{x'}_T} \mathbf{u}_0^P(\mathbf{x'}_T, z_0) \left[\left(\frac{\beta_0}{\alpha_0} - \frac{1}{2} \right) \frac{\delta\rho(\mathbf{x'}_T)}{\rho_0} + 2 \left(\frac{\beta_0}{\alpha_0} \right) \frac{\delta\beta(\mathbf{x'}_T)}{\beta_0} \right] \right\}, \tag{5}$$

$$\mathbf{U}^{SP}(\mathbf{K}_T, z_0) = -ik_\alpha \Delta z \eta^{SP} \hat{k}_\alpha \left\{ \hat{k}_\alpha \cdot \iint d\mathbf{x'}_T e^{-i\mathbf{K}_T \cdot \mathbf{x'}_T} \times \mathbf{u}_0^S(\mathbf{x'}_T, z_0) \left[\left(\frac{\beta_0}{\alpha_0} - \frac{1}{2} \right) \frac{\delta\rho(\mathbf{x'}_T)}{\rho_0} + 2 \left(\frac{\beta_0}{\alpha_0} \right) \frac{\delta\beta(\mathbf{x'}_T)}{\beta_0} \right] \right\}, \tag{6}$$

and

$$\mathbf{U}^{SS}(\mathbf{K}_T, z_0) = -ik_\beta \Delta z \eta^{SS} \hat{k}_\beta \times \left\{ \hat{k}_\beta \times \iint d\mathbf{x'}_T e^{-i\mathbf{K}_T \cdot \mathbf{x'}_T} \times \mathbf{u}_0^S(\mathbf{x'}_T, z_0) \frac{\delta\beta(\mathbf{x'}_T)}{\beta_0} \right\}, \tag{7}$$

where $\hat{k}_\alpha$ and $\hat{k}_\beta$ are unit wavenumber vectors for scattered P- and S-waves, $\delta\alpha$, $\delta\beta$, and $\delta\rho$ are perturbations of P- and S-wave velocities and density (they are all 2D functions obtained from 3D perturbations by taking an integral along the z-direction between z_0 and z_1), ρ_0 is the background density, η^{PP}, η^{PS}, η^{SP}, and η^{SS} are modulation factors with

$$\eta^{PP} = 1, \tag{8}$$

$$\eta^{PS} = \operatorname{sinc}\left[(k_\beta - k_\alpha) \frac{\Delta z}{2} \right] e^{-i(k_\beta - k_\alpha)\Delta z/2}, \tag{9}$$

$$\eta^{SP} = \eta^{*PS}, \tag{10}$$

$$\eta^{SS} = 1, \tag{11}$$

where η^* is the complex conjugate of η, and $\operatorname{sinc}(x) = \sin(x)/x$. Scatterings of the same wave type, i.e., P-P and S-S scatterings, modify P- and S-wave phases. They resemble the scalar-wave phase screen and depend only on P- or S-wave velocity. Scattering between different wave types, i.e., P-S and S-P scattering, involve coupling between P- and S-waves. Coupling terms depend on P-wave velocity, S-wave velocity and density.

Equations 1 to 7 form the basis of the elastic-screen propagator. In equations 4 to 7, the incident waves interact with heterogeneities. These operations are conducted in the horizontal spatial-domain and are very efficient. Then, the spatial-domain results are transformed to the wavenumber domain using fast Fourier transforms. The wavenumber-domain scattered waves given by equations 4 to 7 are substituted into equations 2 and 3. Phase-shift factors in these equations propagate incident and scattered waves passing through the homogeneous background in the wavenumber domain. These wavenumber-domain operations are, again, highly efficient. Finally, plane P- and S-waves in the wavenumber domain are substituted into equation 1 to generate the spatial-domain wavefield using an inverse fast Fourier transform. If turning waves are not of concern, the evanescent wave can be omitted because it does not propagate in the vertical direction. The integral in equation 1 only need be conducted for $\mathbf{K}_T$s that generate real vertical wavenumbers γ_α and γ_β. The above description is focused on a single thin slab. By treating the output from one thin slab as the input of the next slab and iteratively using equations 1 to 7, elastic waves can be propagated through the entire model.

In summary, the model parameters are separated into two parts: the background parameters and the perturbations. The wave propagation through a thin slab is decomposed into a series of steps. The interactions between the incoming waves and the perturbations are conducted in the spatial domain. Plane-wave propagation through the background medium is conducted in the wavenumber domain. In both domains, the calculations are local and highly efficient. There is no time-consuming spatial- or wavenumber-domain convolution involved. The forward and inverse fast Fourier transforms alternate the wavefield between the two domains.

Another advantage of the elastic-screen propagator is that wavefield coupling and propagation are treated separately. As mentioned above, the $\mathbf{U}^{PS}$ and $\mathbf{U}^{SP}$ in equations 2 and 3 represent couplings between P- and S-waves. This gives us the flexibility to turn "on" or "off" certain couplings in the spatial domain. For regions where P- and S-wave velocities change smoothly, we can neglect the coupling between P- and S-waves in equations 4 and 6. If couplings in the entire slab can be omitted, $\mathbf{U}^{PS}$ and $\mathbf{U}^{SP}$ in equations 2 and 3 can be neglected. Using the Rytov approximation, equations 2 and 3 can be rewritten as (Xie and Wu, 2001)

$$\mathbf{u}^P(\mathbf{K}_T, z_1) = e^{i\gamma_\alpha \Delta z} \iint d\mathbf{x'}_T e^{-i\mathbf{K}_T \cdot \mathbf{x'}_T} \mathbf{u}_0^P(\mathbf{x'}_T, z_0) e^{-ik_\alpha \Delta z \delta\alpha/\alpha_0}, \tag{12}$$

$$u^S(\mathbf{K}_T, z_1) = -e^{i\gamma_\beta \Delta z} \hat{k}_\beta \times [\hat{k}_\beta \times \iint d\mathbf{x'}_T e^{-i\mathbf{K}_T \cdot \mathbf{x'}_T} \mathbf{u}_0^S \times (\mathbf{x'}_T, z_0) e^{-ik_\beta \Delta z \delta\beta/\beta_0}. \tag{13}$$

Equations 12 and 13, together with equation 1, form single-wave-type propagators for P- and S-waves. When processing the wavefield extrapolation, based on the model complexity and the migration requirement, we can easily switch to different propagators in different parts of the model. For example, we can use equations 2 and 3 in complex regions with fast velocity changes, use equations 12 and 13 in thick layers with smoothly changing velocities, or turn off wave couplings in salt bodies with nearly constant velocities. If we totally omit coupling between P- and S-waves along the entire propagation path (other than the target reflector), we can use equations 12 and 13 in the entire model. The result will be similar to a converted-wave migration, except here the process is for multicomponent waves, and the polarization information is preserved.

To do the migration, we have to propagate downgoing waves from the source to the target and back propagate reflected waves from the receivers to the target. The propagators derived in this section can be used for forward propagation. The complex conjugates of these propagators can be used for back propagation. Alternatively, one can use the forward propagator together with the time-reversed data (or equivalently, the complex conjugate of the frequency-domain data) to conduct a back propagation. The latter case is equivalent to a reverse-time propagator in the frequency domain, except it is a one-way propagator. The advantage of the latter is that one propagator serves for both up- and downgoing waves (when both of them are in the same wave type). This saves some effort in managing calculations.

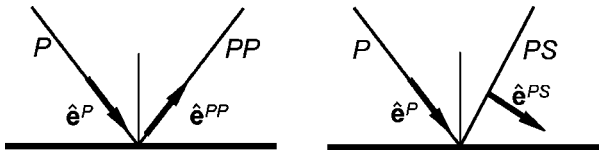

Figure 2. Sign conventions for polarizations. $\hat{\mathbf{e}}^P$, $\hat{\mathbf{e}}^{PP}$, and $\hat{\mathbf{e}}^{PS}$ are polarization vectors for P-, P-P, and P-S-waves, respectively. The reflector is not necessarily horizontal. The P-P and P-S polarization pairs shown in this figure correspond to a positive impedance interface.

WIDE-ANGLE CORRECTION FOR ELASTIC PROPAGATORS

The elastic-screen propagators obtained in the previous section are derived from the perturbation theory and a small-angle approximation. They cannot handle wide scattering angles under large velocity contrasts. However, real situations often contain large velocity contrasts. For scalar waves, several approaches have been employed to improve the accuracy of the screen propagator for large velocity contrasts and wide scattering angles (e.g., Ristow and Ruhl, 1994; Jin et al., 1998a; Xie and Wu, 1998; Huang and Fehler, 2000; Biondi, 2002). A similar method can be adopted for elastic waves (Xie and Wu, 1999). As mentioned previously, the coupling and propagation are calculated separately in screen methods. Having obtained the coupling terms, the P- and S-waves can propagate through the background slab independently; i.e., their propagations are decoupled. This permits us to modify the P- and S-waves separately. The wide-angle correction used for scalar waves can be adopted for elastic waves. To apply the wide-angle correction, screen solutions $\mathbf{u}^P$ and $\mathbf{u}^S$ are first obtained from the coupled equations 2 and 3 or from the single-wave-type equations 12 and 13. Corrections are then performed on $\mathbf{u}^P$ and $\mathbf{u}^S$, respectively. Finally, the corrected results replace $\mathbf{u}^P$ and $\mathbf{u}^S$ in equation 1 to give the modified solution. As for scalar waves, the correction is accomplished by solving an implicit finite-difference problem in the spatial domain (e.g., Ristow and Ruhl, 1994; Jin et al., 1998a; Xie and Wu, 1998, 1999; Huang and Fehler, 2000; Biondi, 2002), which usually gives better stability than the wavenumber-domain method. These processes can fit easily into a dual-domain operation for wavefield extrapolation.

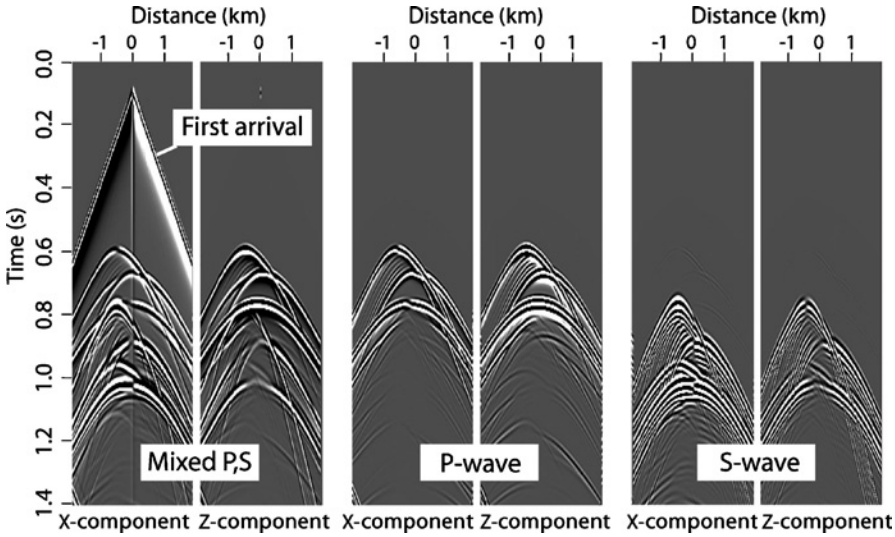

Figure 3. A typical synthetic common-source record. In the left panel is a mixed P- and S-wave record. In the right two panels are the separated pure P- and S-wave records. In each panel, on the left is the horizontal component and on the right is the vertical component. First arrivals are eliminated from the separated P- and S-waves.

IMAGING CONDITIONS

An imaging process is aimed at recovery of interface properties from incident and scattered waves. These properties should not be affected by the configuration of the observation system nor depend on the coordinate system chosen to conduct the calculation. In this study, both up- and downgoing waves are extrapolated using multicomponent screen propagators, and polarizations are preserved throughout the propagation. We developed a vector-imaging condition for the multicomponent-wave imaging. The imaging condition is based on the principle that, at the reflection point, the up- and downgoing waves are in phase (coincidence of incident and reflected waves). This is the same as for scalar waves, except we have two back-propagated upgoing waves, i.e., P-P- and P-S-waves. Following Mittet et al. (1995), the multicomponent imaging conditions for P-P and P-S converted waves can be written as

$$I^{PP}(\mathbf{x}_T, z) = \int C^{P-PP}\left[\hat{\mathbf{e}}^P \cdot \mathbf{u}^P(\mathbf{x}_T, z, \omega)\right] \times \left[\hat{\mathbf{e}}^{PP} \cdot \mathbf{u}^{PP}(\mathbf{x}_T, z, \omega)\right]^* d\omega, \quad (14)$$

and

$$I^{PS}(\mathbf{x}_T, z) = \int C^{P-PS}\left[\hat{\mathbf{e}}^P \cdot \mathbf{u}^P(\mathbf{x}_T, z, \omega)\right] \times \left[\hat{\mathbf{e}}^{PS} \cdot \mathbf{u}^{PS}(\mathbf{x}_T, z, \omega)\right]^* d\omega, \quad (15)$$

where $\mathbf{u}^P$ is the downgoing P-wave from the source, $\mathbf{u}^{PP}$ and $\mathbf{u}^{PS}$ are upgoing P-P and P-S waves back propagated from the receivers, $\hat{\mathbf{e}}^P$, $\hat{\mathbf{e}}^{PP}$, and $\hat{\mathbf{e}}^{PS}$ are the corresponding unit polarization vectors, *denotes the complex conjugate, and C^{P-PP} and C^{P-PS} are normalization factors, which can be chosen from the various versions discussed by Mittet et al. (1995).

Obtaining polarization vectors $\hat{\mathbf{e}}^P$, $\hat{\mathbf{e}}^{PP}$, and $\hat{\mathbf{e}}^{PS}$ is not straightforward. In the frequency domain, the wavefields $\mathbf{u}^P$, $\mathbf{u}^{PP}$, and $\mathbf{u}^{PS}$ are vectors of complex numbers. We can write $\mathbf{u}^P = u^P\,\hat{\mathbf{e}}^P$, $\mathbf{u}^{PP} = u^{PP}\,\hat{\mathbf{e}}^{PP}$, and $\mathbf{u}^{PS} = u^{PS}\,\hat{\mathbf{e}}^{PS}$, where u^P, u^{PP}, and u^{PS} are complex amplitudes. The difficulty is that, unlike real valued vectors, their exact polarization directions cannot be uniquely determined from their components. There is an ambiguity of $\exp(i\pi)$, which can appear in either the amplitudes or the directions of these wavefields. This further introduces ambiguity in the polarization of the image. For easier discussion, we assume that, at the imaging point, both source and receiver waves are linearly polarized. From scattering theory (e.g., Wu and Aki, 1985), the incident and scattered waves form an in-plane problem. The plane is perpendicular to the vector $\hat{\mathbf{e}}^P \times \hat{\mathbf{e}}^{PP}$ or $\hat{\mathbf{e}}^P \times \hat{\mathbf{e}}^{PS}$ and contains the scattering point. Figure 2 shows the P-P and P-S reflection geometry within the plane. Although polarization vectors cannot be uniquely determined, a pair of consistent polarization directions for incident and reflected waves can be obtained. Figure 2 shows polarization pairs for P-P and P-S reflections for a "positive" impedance interface (Aki and Richards, 1980, p. 148). Once polarization pairs are determined, complex wavefields $\mathbf{u}^P$, $\mathbf{u}^{PP}$, and $\mathbf{u}^{PS}$ can be projected onto these directions. Then, correct complex magnitudes can be obtained and applied in the imaging. Taking the P-S-wave image as an example, the process can be summarized as: (a) Find two possible polarization directions for the downgoing P-wave; (b) choose the direction toward the scattering point as $\hat{\mathbf{e}}^P$; (c) find two possible polarization directions for the reflected S-wave; (d) according to the convention shown in Figure 2, choose the correct $\hat{\mathbf{e}}^{PS}$ from the two directions; and, (e) replace $\hat{\mathbf{e}}^P$ and $\hat{\mathbf{e}}^{PS}$ into equation 15 to calculate the P-S image. The imaging condition uses wavefield information at the imaging point. It does not rely on the locations of the source and receivers nor any specific coordinate system. In a complicated wavefield, polarizations are not always perfectly linear. This may cause noise in the image. Summing up contributions from multiple frequencies and sources can reduce these errors.

NUMERICAL EXAMPLES

Synthetic data sets

The multicomponent propagator and imaging conditions are tested here with 2D numerical examples. All synthetic data sets used in this paper are generated using a full-wave, fourth-order, elastic finite-difference algorithm (Xie and Lay, 1994). A P-wave explosion source is used in all calculations.

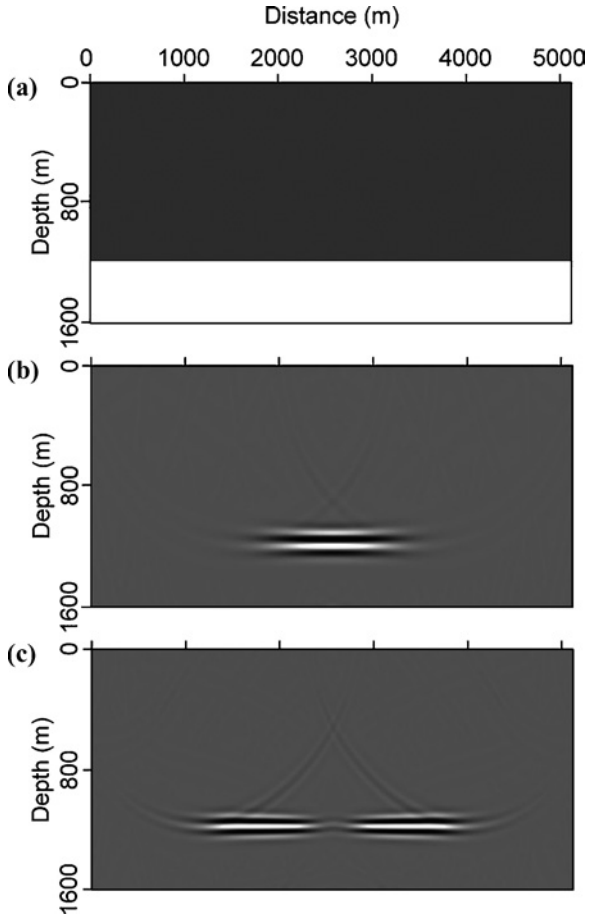

Figure 4. Single-shot prestack imaging. (a) Velocity model, (b) P-P image, and (c) P-S converted-wave image. The velocities and densities are $\alpha_1 = 3.5$ km/s, $\beta_1 = 2.0$ km/s, $\rho_1 = 2.0$ g/cm^3, and $\alpha_2 = 4.5$ km/s, $\beta_2 = 2.4$ km/s, $\rho_2 = 2.2$ g/cm^3, respectively.

To simplify the treatment, absorbing boundaries are used for all sides of the model; no free-surface condition is applied. Before conducting migrations, P- and S-waves are separated by calculating the divergence and curl of the coupled wavefield. The treatment is similar to those used by Zhe and Greenhalgh (1997) and Sun et al. (2001). In our calculation, the separation is performed in the finite-difference code. Direct arrivals have been eliminated from these synthetic data. Figure 3 contains a typical shot record. The separation of P- and S-waves causes some waveform distortions. Zhe and Greenhalgh (1997) and Sun et al. (2001) suggested algorithms for correcting these distortions.

Migration/imaging

All migrations in this section are for common-source data. Single-wave-type propagators, equations 12 and 13, combined with wide-angle modifications, are used for both the downgoing P-wave and the upgoing P-P and P-S waves. An explosive P-wave source is used at the first screen to generate a downgoing wavefield. Equations 14 and 15 are used for imaging. In cases where multiple sources are used, partial images from different sources are stacked for obtaining the final image.

Simple model with one reflector

The first example is a simple, two-layer velocity model (Figure 4a). A single shot is located at the center on the surface. There are 400 receivers located on the surface with offsets from -2000 to 2000 m. For calculating synthetic data, $dx = dz = 5$ m and $dt = 0.8$ ms. For migration, we use $dx = dz = 10$ m and $dt = 8$ ms. Figures 4b and c contain the P-P image and the P-S converted-wave image, respectively. Both images reveal the interface. Several features can be seen from this simple model. Since the S-wave scattering angle is smaller than that of the P-wave, the P-S image has a wider angle coverage. With the application of the vector-imaging condition, the converted-wave image has the correct polarization on both sides of the source. This allows us to construct the image by stacking results from multiple sources. Because of the shorter wavelength of the *S*-wave, the resolution of the P-S image is slightly higher than that of the P-P image.

Three-layer model

The second example is a three-layer model (Figure 5). Sixteen shots on the surface are used to illuminate the structure. Their locations are shown in Figure 5a. Each shot has 160 receivers with offsets from -1600 to 1600 m. To calculate synthetic seismograms using the finite-difference method, we used a grid with $dx = dz = 5$ m and $dt = 0.5$ ms. For the migration, a grid with $dx = dz = 20$ m and $dt = 4$ ms is used. The stacked P-P image and P-S converted-wave image are shown in Figures 5b and c, respectively. As a consequence of the vector-image condition, converted-wave images from each shot can be directly stacked to generate the final P-S wave image. Both P-wave- and converted-wave image qualities are

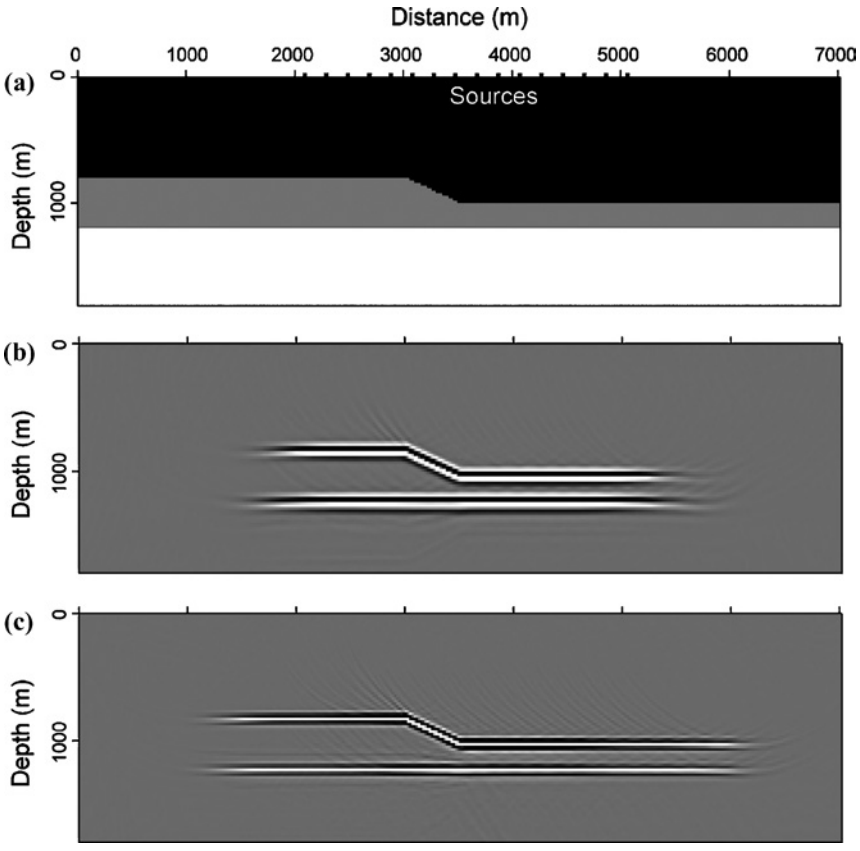

Figure 5. Migrated images of a three-layer model. (a) Velocity model, (b) P-P image, and (c) P-S converted-wave image. The velocity and density parameters are $\alpha_1 = 3.5$ km/s, $\beta_1 = 2.0$ km/s, $\rho_1 = 2.0$ g/cm^3, $\alpha_2 = 4.0$ km/s, $\beta_2 = 2.4$ km/s, $\rho_2 = 2.2$ g/cm^3, and $\alpha_3 = 4.5$ km/s, $\beta_3 = 2.6$ km/s, $\rho_3 = 2.4$ g/cm^3, respectively. Sixteen shots are used to illuminate the model. Note that partial images from individual shots are correctly stacked to generate a P-S converted-wave image.

good. As in Figure 4, the P-S-wave image shows slightly higher resolution.

Two-dimensional elastic SEG/EAGE salt model

The next model is a modified version of a 2D slice through the SEG/EAGE salt model (O'Brien and Gray, 1996; Aminzadeh et al., 1997). The original salt model is an acoustic model with only sound-wave speed. To make this model suitable for elastic modeling/migration, several modifications have been made. The sound-wave speed is used as the P-wave speed. The S-wave speed is obtained from the P-wave speed by assuming Lamé constant $\lambda = \mu$ or, equivalently, $\alpha = 1.73\beta$. The density ρ can be determined based on Gardner et al.'s (1974) relation (Sheriff, 1991, p. 135) or Birch's law (see, for example, Fowler, 1990, p. 78; Sheriff, 1991, p. 27). Our current elastic finite-difference code does not handle a water layer with $\mu = 0$. We eliminated the top water layer in the original SEG/EAGE salt model by filling it with a layer of material with similar properties to the subwater layer. Figure 6a shows the P-wave velocity of the modified model. A velocity grid with $dx = dz =$ 6 m and $dt = 1$ ms is used to generate the synthetic data set, while a grid with $dx = dz =$ 24 m and $dt = 8$ ms is used for multicomponent migration. On the surface, 120 shots are used to illuminate the structure (as a comparison, the original 2D acoustic data set is composed of 325 shots). For each shot, we used 160 receivers with offsets from −1950 to 1950 m.

The migrated P-P and P-S images are shown in Figures 6b and c, respectively. The salt body is well imaged, as is the flat reflector at the bottom of the model. Thus, even with the existence of a high-speed salt body, the wide-angle propagator correctly extrapolates P- and S-waves to the bottom of the model. Generally, the P-P image is better than the P-S image, because a reflected P-wave usually has more energy. In the subsalt region, the incident angle for the incoming P-wave is small (near-perpendicular incidence) and the P to S reflection is weak. This causes very weak converted-wave images for many of the subsalt structures. Weak coherent noise can be seen both inside and below the salt body; these coherent noise are mainly from locally converted waves in the up- and downgoing legs.

DISCUSSION

The current study focuses on the multicomponent screen propagator and the vector-image conditions. The separation of P- and S-waves is simply performed within the finite-difference code used for generating synthetic data. For field data, the separation of P- and S-waves from multicomponent records is an important issue. Both Zhe and Greenhalgh (1997) and Sun et al. (2001) have suggested using a full-wave elastic, finite-difference, reverse-time propagator to extrapolate the mixed wave downward for a small distance. Then separate P- and S-waves within the finite-difference code by calculating the divergence and curl of the displacement field. This technique can also solve the free-surface condition. Other techniques also are proposed to solve the P- and S-wave separation (e.g., Amundsen and Reitar, 1995; Jin et al. 1998b). Theoretically, these methods can be used for processing field data. However, their robustness has yet to be tested.

All the numerical examples tested in this paper are conducted using the single-wave-type propagators in 2D models. However, the formulation presented in this research is for full 3D migration and includes coupled waves. Although only a P-wave source is discussed in this paper, S-wave sources, or sources generating mixed P- and S-waves, can be easily

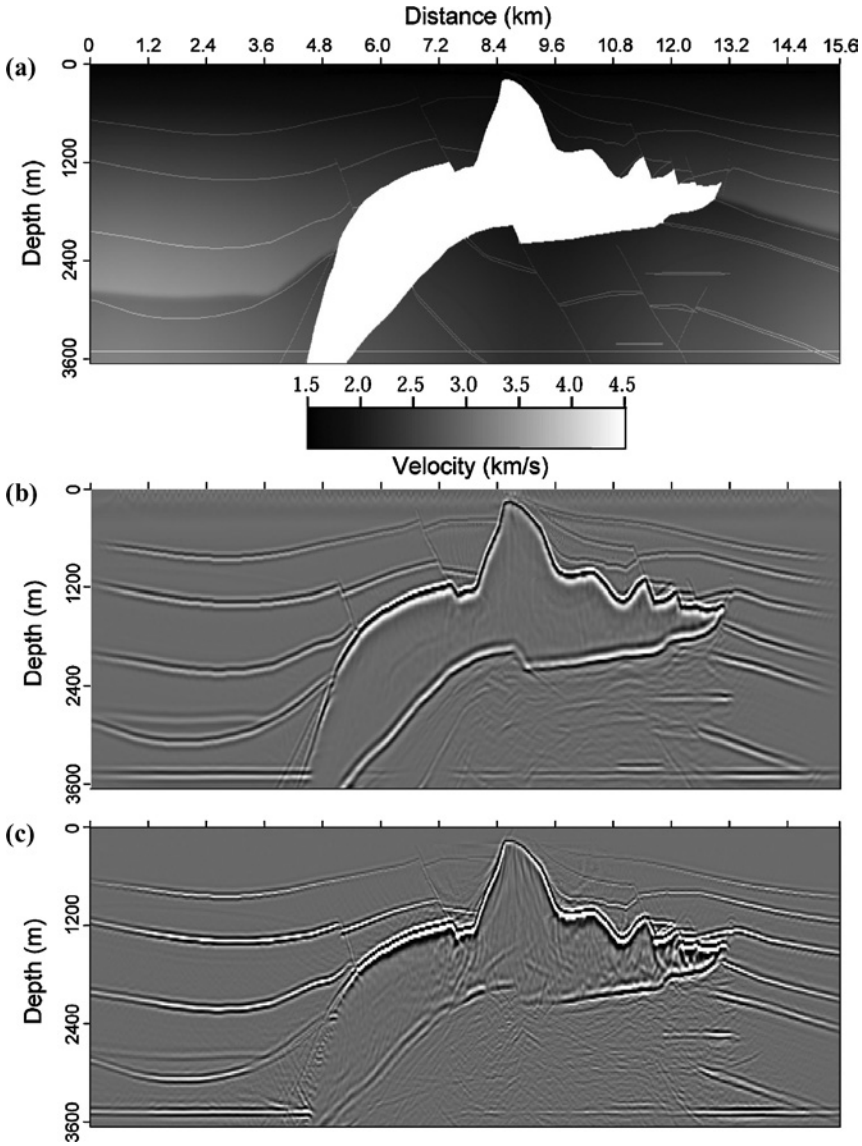

Figure 6. Migrated images of the elastic SEG/EAGE salt model. (a) Modified velocity model (P-wave), (b) P-P image, and (c) P-S converted-wave image.

included. Imaging conditions for S-wave incidence can also be derived. In our numerical examples, both sources and receivers are located at the same depth in the model, but the current method also works where sources and receivers are located at different depths. For example, sources can be near the surface, while the receivers lie on the ocean bottom or are in vertical cables.

CONCLUSION

The elastic-screen method based on the one-way wave equation is used for multicomponent prestack depth migration. Wave equation–based propagators are used for both up- and down-going waves. The method avoids problems usually related to the high-frequency asymptotic approach, e.g., caustics and multipathing. Compared with methods using a scalar-wave propagator for elastic migration, our method preserves the polarization information in multicomponent waves. Vector-imaging conditions, combined with polarization information, can automatically give the correct sign of the converted-wave image, which makes stacking of partial images from separate sources straightforward. This method requires that the P- and S-waves be separated before the wavefield extrapolation. The screen propagator is a very efficient wave-propagation method. For scalar waves, it has been successfully used in prestack depth migration. Conducting multicomponent migration using the elastic-screen propagator should be within the processing power of current-day computers.

ACKNOWLEDGMENTS

We sincerely thank Professors Paul Stoffa and Stewart Greenhalgh, and two other reviewers for their comments, which considerably improved our manuscript. This research is supported by the Department of Energy under Grant No. DE-FG03-01ER15144. Facility support from the W. M. Keck Foundation is also acknowledged. Contribution No. 445 of the Center for the Study of Imaging and Dynamics of the Earth, Institute of Geophysics and Planetary Physics, University of California, Santa Cruz.

REFERENCES

Aki, K., and P. G. Richards, 1980, Quantitative seismology, Theory and methods, Vol. I: Freeman and Company.

Aminzadeh, F., J. Brac, and T. Kunz, 1997, SEG/EAGE 3-D salt and overthrust models, in SEG/EAGE 3-D Modeling Series, No. 1: SEG.

Amundsen, L., and A. Reitar, 1995, Extraction of P- and S-waves from the vertical component of the particle velocity at the sea floor: Geophysics, **60**, 231–240.

Biondi, B., 2002, Stable wide-angle Fourier finite-difference downward extrapolation of 3-D wavefields: Geophysics, **67**, 872–882.

Chang, W. F., and G. A. McMechan, 1987, Elastic reverse-time migration: Geophysics, **52**, 1367–1375.

Chang, W. F., and G. A. McMechan, 1994, 3-D elastic prestack reverse-time depth migration: Geophysics, **59**, 597–609.

Dai, T. F., and J. T. Kuo, 1986, Real data results of Kirchhoff elastic wave migration: Geophysics, **51**, 1006–1011.

Fisk, M. D., and G. D. McCartor, 1991, The phase screen method for vector elastic waves: Journal of Geophysical Research, **96**, 5985–6010.

Fowler, C. M. R., 1990, The solid earth, An introduction to global geophysics: Cambridge University Press.

Gardner, G. H. F., L. W. Gardner, and A. R. Gregory, 1974, Formation velocity and density—the diagnostic basics for stratigraphic traps: Geophysics, **39**, 770–780.

Hokstad, K., 2000, Multicomponent Kirchhoff migration: Geophysics, **65**, 861–873.

Hou, A., and K. J. Marfurt, 2002, Multicomponent prestack depth migration by scalar wavefield extrapolation, Geophysics, **67**, 1886–1894.

Huang, L. J., M. C. Fehler, and R. S. Wu, 1999, Extended local Born Fourier migration method: Geophysics, **64**, 1524–1534.

Huang, L. J., and M. C. Fehler, 2000, Globally optimized Fourier finite-difference migration method: 70th Annual International Meeting, SEG, Expanded Abstracts, 802–805.

Jin, S., R. S. Wu, and C. Peng, 1998a, Prestack depth migration using a hybrid pseudo-screen propagator: 68th Annual International Meeting, SEG, Expanded Abstracts, 1819–1822.

Jin, S., R. S. Wu, X. B. Xie, and Z. Ma, 1998b, Wave equation-based decomposition and imaging for multicomponent seismic data: Journal of Seismic Exploration, **7**, 145–158.

Kuo, J. T., and T. F. Dai, 1984, Kirchhoff elastic wave migration for the case of noncoincident source and receiver: Geophysics, **49**, 1223–1238.

Mittet, R., R. Sollie, and K. Hokstad, 1995, Prestack depth migration with compensation for absorption and dispersion: Geophysics, **60**, 1485–1494.

O'Brien, M. J., and S. H. Gray, 1996, Can we image beneath salt: The Leading Edge, **15**, 17–22.

Ristow, D., and T. Ruhl, 1994, Fourier finite-difference migration: Geophysics, **59**, 1882–1893.

Sheriff, R. E., 1991, Encyclopedic dictionary of exploration geophysics, Third ed.: Society of Exploration Geophysicists.

Stoffa, P. L., J. T. Fokkema, R. M. D. Freire, and W. P. Kessinger, 1990, Split-step Fourier migration: Geophysics, **55**, 410–421.

Sun, R., and G. A. McMechan, 2001, Scalar reverse-time depth migration of prestack elastic seismic data: Geophysics, **66**, 1519–1527.

Sun, R., J. Chow, and K. J. Chen, 2001, Phase correction in separating *P*- and *S*-waves in elastic data: Geophysics, **66**, 1515–1518.

Wild, A. J., and J. A. Hudson, 1998, A geometrical approach to the elastic complex screen: Journal of Geophysical Research, **103**, 707–725.

Wu, R. S., 1994, Wide-angle elastic wave one-way propagation in heterogeneous media and an elastic wave complex-screen method: Journal of Geophysical Research, **99**, 751–766.

Wu, R. S., 1996, Synthetic seismograms in heterogeneous media by one-return approximation: Pure and Applied Geophysics, **148**, 155–173.

Wu, R. S., and K. Aki, 1985, Scattering characteristics by an elastic heterogeneity, Geophysics, **50**, 582–595.

Wu, R. S., and X. B. Xie, 1994, Multi-screen back propagator for fast 3D elastic prestack migration: Mathematical Methods in Geophysical Imaging II, International Society for Optical Engineering (SPIE), **2301**, 181–193.

Xie, X. B., and T. Lay, 1994, The excitation of Lg waves by explosions: A finite-difference investigation: Bulletin of the Seismological Society of America, **84**, 324–342.

Xie, X. B., and R. S. Wu, 1996, 3D elastic wave modeling using the complex screen method: 66th Annual International Meeting, SEG, Expanded Abstracts, 1247–1250.

Xie, X. B., and R. S. Wu, 1998, Improve the wide angle accuracy of screen method under large contrast: 68th Annual International Meeting, SEG, Expanded Abstracts, 1247–1250.

Xie, X. B., and R. S. Wu, 1999, Improve the wide angle accuracy of the screen propagator for elastic wave propagation: 69th Annual International Meeting, SEG, Expanded Abstracts, 1863–1866.

Xie, X. B., and R. S. Wu, 2001, Modeling elastic wave forward propagation and reflection using the complex screen method: Journal of the Acoustic Society of America, **109**, 2629–2635.

Xie, X. B., C. C. Mosher, and R. S. Wu, 2000, The application of wide angle screen propagator to 2D and 3D depth migrations: 70th Annual International Meeting, SEG, Expanded Abstracts, 878–881.

Zhe, J., and S. A. Greenhalgh, 1997, Prestack multi-component migration: Geophysics, **62**, 598–613.